Supplement of Biogeosciences Discuss., 11, 16599–16643, 2014
http://www.biogeosciences-discuss.net/11/16599/2014/
doi:10.5194/bgd-11-16599-2014-supplement

Biogeosciences
Discussions
Open Access

Supplement of

Observation-based modelling of permafrost carbon fluxes with accounting for deep carbon deposits and thermokarst activity

T. Schneider von Deimling et al.

Correspondence to: T. Schneider von Deimling (schneider@pik-potsdam.de)

Supplementary material

1 Model initialization

1.1 Permafrost carbon inventory

Based on updated soil carbon data (Hugelius et al., 2013) we describe the amount of organic matter in near-surface permafrost which we allocate into a mineral soil pool (SOCC<20% per weight, 540 Pg-C) and into an organic soil pool (SOCC>20%, 120 Pg-C), separately for the depth levels 0 to 1m, 1 to 2m, and 2 to 3m. We hereby focus on carbon in permafrost-affected soils, i.e. orthels and turbels for the mineral pools, and histels for the organic pools (see Fig. 1). Furthermore, we consider two additional pools to describe carbon stored in ice-rich deep deposits ranging from the surface to a depth of 15 meters. Following the inventory classification by Strauss et al. (2013), we consider a Yedoma pool (~80 Pg-C, 0 to 15m) and a refrozen thermokarst pool (~130 Pg-C, 0 to 5m). To avoid double-accounting of near-surface inventory estimates, we subtract the amount of permafrost carbon in the top three meters of the Yedoma and refrozen thermokarst pools (Strauss et al., 2013) from the near-surface mineral soil pool (Hugelius et al., 2013). While the Yedoma pool classifies carbon deposits unaffected by past thermokarst activity, the refrozen thermokarst pool describes organic material buried in sediments which had been subject to abrupt permafrost thaw in the past. In addition to the estimate of Yedoma and thermokarst carbon deposits by Strauss et al. (2013), we also consider permafrost carbon stored in deep taberal sediments (~110 Pg-C, Walter-Anthony et al., 2014) in the depth range 5 to 15m (Fig.1). We do not separately consider an estimated 70 Pg-C stored perennially frozen in deep deltaic alluvium (Hugelius et al., 2014). The potential for intensive future thermokarst formation (and thus for deep thaw) in typical deltaic landscapes is rather small, thus we assume that a large portion of this deep carbon store will remain frozen over the next centuries.

As we start our simulations from pre-industrial climate, we enlarge our data-based near-surface carbon pools by 10%. This increase accounts for historical permafrost carbon release and matches the amount of simulated permafrost carbon at the year 2000 with the inventory estimates by Hugelius et al. (2014).

1.2 Permafrost temperatures and active layer profile

To fully initialize our model, we had to determine permafrost ground temperatures of our carbon inventory. Actual observations, however, are limited and we therefore make the simplifying assumption that ground temperatures are to first order determined by surface air temperatures. We used climatology data from the Berkeley Earth dataset (http://berkeleyearth.org/data) to partition our permafrost grid cells (which range from 47°N to 84°N) into bins of varying surface air temperatures[1]. Based on typical north-south gradients of mean annual ground temperatures (MAGTs) (Romanovsky et al., 2010;Beer et al., 2013), we assume that the bin with the warmest air temperatures corresponds to southern and warm permafrost with an initial MAGT of –0.5°C ($MAGT_{Max}$), and that the bin with coldest air temperatures corresponds to northern permafrost with an initial MAGT of –10°C ($MAGT_{Min}$). For our default parameter setting, we linearly scale the remainder of temperature bins between $MAGT_{Max}$ and $MAGT_{Min}$. To account for uncertainty, we use a non-linear scaling to allow for clustering towards warmer or colder initial MAGTs (with keeping the total range of –10°C to –0.5°C fixed).

After initialization, MAGT is re-calculated at each time-step for each depth level between the soil surface and the active layer depth by assuming a time-lagged response of soil temperatures to changing surface air temperatures. Hereby we assume an increasing lag with depth, i.e. a maximum lag at the active layer level which decreases towards zero at the soil surface.

We determine the latitudinal profile of the active layer based on our prescribed north-south gradient of initial MAGTs. We assume the seasonal ground temperature cycle to exponentially decay with depth and we choose a typical scale depth to infer temperature profiles consistent with observed, “trumpet-shaped” soil temperature profiles (Romanovsky et al., 2010;Boike et al., 2013).We then define the equilibrium active layer level for each soil pool and for each latitude as the depth at which maximum soil summer temperatures equal zero degrees. Warmer locations or stronger seasonal cycles result in deeper active layers than colder regions or locations of reduced annual temperature ranges (see Koven et al. (2013)).

[1] We use summer air temperatures because they are likely to result in a better representation of the soil thermal state compared to annual mean air temperatures. Cold winter air temperatures do not fully penetrate into the ground because snow cover is an effective thermal insulator.

2 Thaw rate parametrization

We model the process of long-term active layer deepening by assuming that thaw rates can be parametrized depending on four key factors: thermal ground properties, mean annual ground temperatures, active layer depth, and magnitude of the regional warming anomaly which drives permafrost degradation. For each latitude band *lat*, soil type *S*, and aerobic/anaerobic regime *A*, we separately calculate the time evolution of active layer depths by describing individual thaw rates $TR(t)$:

$$TR(t)_{S,A,lat} = \bar{\alpha}_{S,A} * S(t)_{S,A,lat} * \frac{dT^*(t)_{A,lat}}{z_{ALD}(t)_{S,A,lat}} \qquad (1),$$

with $\bar{\alpha}$ describing aggregated soil-specific thermal diffusivities, $S(t)$ a soil temperature dependent scaling, $dT^*(t)$ the thaw driving surface warming anomaly, and $z_{ALD}(t)$ the active layer depth. The choice for these four factors is motivated in the following:

1) $\bar{\alpha}_{S,A}$ is a soil-specific parameter (*aggregated thermal diffusivity*) which determines how effectively heat can penetrate into the ground. Hereby we assume that heat diffusion into the frozen ground is to first order determined by the ice content of the sediments. We first prescribe $\bar{\alpha}_S$ for mineral soils under aerobic conditions and then use scaling factors to infer thermal diffusivities for the remaining carbon pools. As the high latent heat content of ice-rich deposits impedes the rate of downward thawing (Jorgenson et al., 2010, Romanovsky et al., 2010), we scale $\bar{\alpha}_S$ according to assumed ice-contents (typical mineral soils: 25 vol%, Yedoma: 70 vol%, refrozen thermokarst: 45 vol% (Schirrmeister et al., 2011;Strauss et al., 2013). For organic soils we assume a reduced thermal diffusivity compared to mineral soils (factor 0.5) given higher ice-contents and the low thermal conductivity of organic matter. When lakes grow deep enough to prevent winter re-freeze, permafrost degradation increases substantially due to year-round thawing (Arp et al., 2012). To capture the increase in thaw rates after thermokarst formation, we tune $\bar{\alpha}_{S,A}$ to match simulated talik propagation of Kessler et al. (2012). If soils are subject to wetland conditions (i.e. they are moisture-saturated but are not covered by lakes), we assume a reduced thermal diffusivity given the higher ice contents in these soils (see Table 1).

2) When permafrost is close to zero degrees, almost all heat is used for the phase transition from ice to water, while for colder conditions the majority of the warming anomaly is used to increase permafrost temperatures with little downward propagation of the thaw front. To capture the difference between much lower thaw rates in cold as compared to warm permafrost (see Schaphoff et al. (2013)), we describe a latitude-dependent scaling factor $S(t)_{lat}$ which non-linearly scales thaw rates by mean annual ground temperatures (MAGTs). Hereby, we describe a quartic dependency of $S(t)_{lat}$ on MAGT to capture the sharp increase in thaw rates when permafrost temperatures approach zero degrees. The scaling factor profile is parametrized to yield a ratio of 1:10 for thaw rates at coldest (MAGT= –10°C) to warmest (MAGT=0°C) permafrost.

3) We capture the strong dampening of heat propagation with depth by assuming that the thaw rate is inversely proportional to depth (Kessler et al., 2012). This allows us to reproduce the general tendency of high talik development rates in the first years after thermokarst initiation and gradual decrease with time (Ling, 2003).

4) The magnitude of the regional surface warming anomaly is a further key driver of subsurface permafrost degradation. We assume thaw rates in non-thermokarst affected sediments being proportional to the magnitude of the surface air temperature anomaly, i.e. the warming above pre-industrial temperatures. We calculate the warming anomaly in each latitude band by accounting for the length of the thaw season (i.e. by the yearly fraction of days with non-freezing surface air temperatures). To account for key differences in thaw rates between non-thermokarst and thermokarst-affected sediments, we assume that degradation of the latter is driven over a full year by lake bottom temperatures (and thus not by seasonal surface air temperatures). We calculate lake bottom temperatures based on the annual cycle of surface air temperatures while assuming that the annual summer amplitude is damped by 50% (Boike et al., 2013) and that winter lake bottom temperatures cannot fall below a minimum of two degrees Celsius.

To ensure that our scheme for describing permafrost thaw dynamics yields robust results, we perform at each time step a consistency check: we calculate the equilibrium active layer depth which would establish under the given climatic boundary conditions (determined by mean annual air temperature and the amplitude of the seasonal cycle). We use this depth as a constraint for maximum thaw rates and thus assure that the parametrization of thaw rates yields physically plausible results.

3 Anaerobic soil fractions

3.1 Thermokarst lake pool

To capture future thermokarst dynamics, we have developed a conceptual model of thermokarst formation and drainage. Our simulation approach is chosen to test different hypotheses of future thermokarst evolution rather than providing a deterministic model projection based on small-scale thermokarst processes (such as e.g. Kessler et al. (2012), Ling et al. 2012). To keep our model description as simple as possible, we assume that future increases in surface air temperatures are the main driver for thermokarst formation through melting of near-surface ground ice and subsequent ground subsidence. Moreover, we neglect factors other than temperature (e.g. surface disturbance, precipitation or local topography) which also can affect thermokarst formation (van Huissteden et al., 2011).

To describe the evolution of newly formed thermokarst lakes in each latitudinal band, we use an optimum function which non-linearly scales the latitudinal thermokarst lake area fraction $F^{TKL}(t)$ by the surface air temperature anomaly $d\bar{T}'(t)$ (see Fig. S1):

$$F^{TKL}{}_{S,lat}(t) = d_S * \exp(a_S * d\bar{T}'(t) - b_S * d\bar{T}'(t)^{c_{lat} * d\bar{T}'(t)}) \tag{2}$$

For each soil pool $F^{TKL}(t)$ describes the area fraction per latitudinal band which is affected by newly formed thermokarst lakes. The high-latitude surface air temperature anomaly $d\bar{T}'(t)$ drives changes in thermokarst lake extent. It is defined as the annual surface air warming above pre-industrial temperatures, averaged over all permafrost regions. We infer $d\bar{T}'(t)$ based on an analysis of polar amplification factors from state-of-the-art climate models (CMIP-5, (Taylor et al., 2011). With rising $d\bar{T}'(t)$, $F^{TKL}(t)$ increases towards an optimum at which the maximum thermokarst lake fraction F^{TKLmax} is realized at $d\bar{T}'^{TKLmax}$. With further warming above $d\bar{T}'^{TKLmax}$ drainage and additional processes (such as increasing evaporation and terrestrialization (van Huissteden and Dolman, 2012)) are assumed to outweigh lake formation.

By our model design, further warming above $d\bar{T}'^{TKLmax}$ leads to a decrease in the thermokarst lake area which cannot fall below a prescribed minimum area fraction F^{TKLmin}. We prescribe a decline which is most pronounced in southern permafrost regions where we assume a minimum fraction of remaining lakes F^{TKLmin} of 3% (see Fig. S1). In the coldest permafrost regions we assume a minimum fraction of 15%. The latitudinal gradient expresses the potential for more extensive drainage at the southern, discontinuous permafrost boundary where the permafrost body is thin and where internal drainage (i.e. subterraneous outflow (Yoshikawa and Hinzman, 2003)) is an efficient pathway for water removal. In northern, continuous permafrost regions, we only consider lateral erosion through thermo-erosional landforms and expansion of lakes in thermokarst basins (Morgenstern et al., 2011) an efficient drainage mechanism. We determine the soil-specific shape parameters a_S, b_S, d_S by prescribing F^{TKLmax} and $d\bar{T}'(t)$ for each carbon pool individually (see Table 1).

In specific regions, about 80% of the landscape is affected by thermokarst and thermal erosion (Strauss et al., 2013). Yet it is unlikely that future thermokarst coverage will be as extensive because existing degradational landforms and other topographic lows will favour future lake drainage (Morgenstern et al. 2011). We assume the highest potential for new thermokarst lake formation in unaltered ice-rich Yedoma sediments which had not been affected by past thermokarst activity. We further assume a reduced potential for the formation of second-generation lakes in existing basins (Morgenstern et al. 2011), i.e. in refrozen thermokarst deposits. The lowest potential of new thermokarst lake formation is assumed for less ice-rich organic and mineral soils (see Table 1).

By newly formed lakes we consider thermokarst lakes which establish under temperatures warmer than pre-industrial. We do not consider existing thermokarst lakes (formed over the last centuries to millennia) as a part of our thermokarst lake pool. These lakes have likely formed deep taliks in the past and are underlain by sediments potentially depleted in labile organic matter. We further only consider lakes being part of our thermokarst pool if they are deep enough to prevent winter refreeze of the lake bottom waters (about 1 to 2m (Arp et al., 2012;Yi et al., 2014)). As we do not model lake depth expansion we assume that formation of new thermokarst lakes is initiated for any warming above our reference climate (i.e. pre-industrial climate), while we also assume that extensive talik formation under thermokarst lakes is only realized after newly formed lakes have deepened enough to reach the critical depth which prevents winter refreeze (we define this time to be the year 2000). Arctic landscapes are also covered by numerous smaller lakes or ponds which fully refreeze in winter and do not develop deep taliks. Therefore they do not provide conditions for abrupt permafrost degradation and we consider ponds and smaller lakes part of our wetland pool.

We do not account for changes of the CO_2 and CH_4 flux balance through establishment of new vegetation after drainage (van Huissteden and Dolman, 2012;Kessler et al., 2012;Jones et al., 2012;Walter Anthony et al., 2014), see discussion in section model limitations).

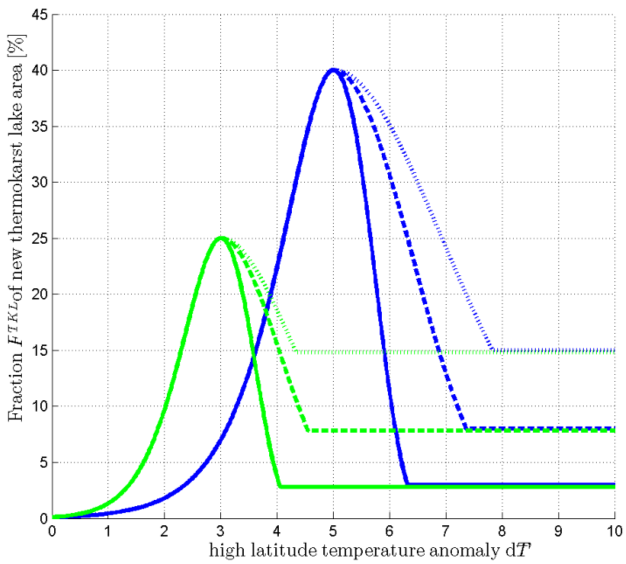

Fig.S1: Temperature dependency of newly formed thermokarst lake area fractions. The figure illustrates the increase and decrease of the new thermokarst lake area fraction F^{TKL} (as percentage of the total permafrost area in each latitude band) with rising high latitude surface air warming $d\overline{T}'$. Curves are shown for two different choices of maximum thermokarst lake extents F^{TKLmax} (green: 25%, blue: 40%) and corresponding warming $d\overline{T}'^{TKLmax}$ (green: 3°C, blue: 5°C). The different line styles illustrate the latitudinal dependency of drainage for warming above $d\overline{T}'^{TKLmax}$ (solid: southern permafrost limit, dashed: mid permafrost latitude, dotted: northern permafrost limit).

3.2 Wetland pool

In this study we assume that high latitude wetland extent will slightly increase over the near-term with future warming. Such an assumption is supported by projected increases in the hydrologic balance of precipitation minus evaporation (AICA, Wash et al., chapter 6, 2009). We do not investigate a scenario of potential northern wetland drying (as e.g. investigated by Avis et al. (2011)). In our model setting we describe an increase in the wetland area fraction per latitude band by a linear scaling with high latitude warming, i.e. with the high-latitude surface air temperature anomaly $d\overline{T}'(t)$. Each carbon pool is initialized with a minimum wetland extent at pre-industrial temperatures and reaches its maximum extent for a high-latitude warming $d\overline{T}'$ of 10°C (see Table 1). For further warming the wetland fraction is kept constant at the maximum extent.

Our simulated wetland CH_4 fluxes describe methane produced from newly thawed permafrost carbon. Yet the full carbon balance of wetlands is rather complex and possibly more affected by future changes in soil moisture, soil temperature, and vegetation composition than by the delivery of newly thawed organic matter through permafrost degradation (Olefeldt et al., 2013). The accounting of these additional factors requires the implementation of comprehensive wetland models (such as formulated by (Kleinen et al. (2012);Frolking et al. (2001)).

4 Carbon release

Based on our thaw rate parametrization (equation 1), we track the active layer depth for each pool at each time step and thus can calculate the amount of carbon which is thawed as a consequence of warming above pre-industrial temperatures. We refer to this newly thawed carbon as vulnerable carbon VC(t) (Burke et al., 2012). Carbon release $C^{\uparrow}(t)$ for each soil carbon pool S, aerobic/anaerobic environment A, organic matter quality Q, latitude lat, and depth level z is assumed proportional to the pool-specific amount of vulnerable carbon $VC(t)$ and release rate R(t) (see Table 1):

$$C^{\uparrow}{}_{S,A,Q,lat,z}(t) = R_{S,A,Q,lat,z}(t) * VC_{S,A,Q,lat,z}(t) \quad (3)$$

We do not explicitly account for gaseous transport from subsoil layers to the atmosphere but assume that the timescale involved is small compared to CO_2 and CH_4 production. Therefore, we assume that carbon release rates can be described by CO_2 and CH_4 production rates. Yet we account for pool-specific oxidation during methane release. We hereby assume little oxidation of CH_4 from thermokarst sediments because ebullition is a rather effective pathway with little chance for CH_4 oxidation. To the contrary, CH_4 release from wetlands is likely affected much stronger by oxidation. We therefore assume systematically higher oxidation rates for these soils (see Table 1).

Under anaerobic degradation of organic matter, methane can be produced via a variety of complex food webs (Segers, 1998). For our fast pool (which describes labile organic matter) we assume that methane production is dominated by fermentation of acetate. Given the stoichiometry of CH_4 production by methanogenesis via this pathway, we assume a 1:1 production ratio of CH_4:$CO_2^{anaerobic}$ (Walter Anthony et al., 2014;Conrad et al., 2002). Incubations studies suggest this ratio can deviate strongly from 1:1 and cover very large ranges with anaerobic CO_2 production one to two orders of magnitude larger than CH_4 production (Lee et al., 2012;Scanlon and Moore, 2000;Segers, 1998). We do not account for very low CH_4:$CO_2^{anaerobic}$ ratios (<0.07) which might be explained by high initial CO_2 production and a strong decline with time after which a stable, much larger CH_4:$CO_2^{anaerobic}$ ratio might establish (Scanlon and Moore, 2000).

Compared to the amount of labile organic matter, the slow carbon pools describe a much larger inventory of organic material of varying compositions and structures. We assume that methane production can also follow alternative pathways under which alternative electron acceptors are likely becoming important which can reduce CH_4:$CO_2^{anaerobic}$ production ratios. Based on incubation results from Lee et al. (2013), we assume an anaerobic production ratio CH_4:$CO_2^{anaerobic}$ of 1:7 (±50%) for organic matter in the slow pool (Table 1).

As microbial soil activity rises with increasing soil temperatures, we account for a Q_{10} temperature sensitivity of carbon decomposition: we calculate carbon release rates $R(\mathrm{t})$ for each carbon pool, each latitude, and each vertical layer by scaling CO_2 and CH_4 production rates P by monthly soil temperatures $TS(t)$:

$$R_{S,A,Q,lat,z}(t) = (1 - OX_A) * (P_{A,Q} * Q_{10\,A}{}^{(TS_{S,A,lat,z}(t)-10)/10}) \quad (4)$$

We calculate monthly soil temperature *TS(t)* by assuming an exponential decay of the seasonal temperature cycle with depth. We hereby assume a lagged temperature response with time (i.e. zero lag at the soil surface which is assumed to warm at the same rate as surface air and maximum lag at the active layer depth). When soil temperatures drop below zero degrees we assume soil microbial activity to be negligible and decomposition is halted. $(1 - OX_A)$ describes the fraction of released carbon which is not oxidized (with $OX = 0$ for CO_2, and $OX = OX_{WET}$ or $OX = OX_{TKL}$ for CH_4, see Table 1).

5 Carbon-cycle and climate model

To close the feedback loop of warming-induced permafrost degradation, carbon release, and additional warming, we use a simple multi-box carbon-cycle climate model from Allen et al. (2009) which was designed to span the full range of temperature and carbon cycling dynamics consistent with observations.

The model calculates atmospheric CO_2 concentrations by describing a diffusive uptake of emitted CO_2 through vegetation and surface oceans, and by an advective carbon transport into the deep ocean. The uptake of heat by the ocean is modelled by a diffusive process. We have used the model description by Allen et al. (2009) and have extended their model design by describing a declining diffusive CO_2 uptake with rising temperatures. The extended diffusive description allows us to model a decrease in airborne fractions with rising temperatures inferred from complex models (Friedlingstein et al., 2006). We have tuned model parameters such that we could reproduce individual CO_2 concentration pathways from the RCP database (www.iiasa.ac.at/web-apps/tnt/RcpDb, Meinshausen 2011) based on CO_2 emission trajectories of all four standard RCPs. To calculate deviations in atmospheric methane concentrations, we assume an exponential decay of CH_4 anomalies with a typical e-folding lifetime of 11 years.

We calculate radiative forcing of CO_2 and of CH_4 by using standard formulae after Myhre et al. (1998). Hereby, we also assume that indirect methane effects lead to a radiative forcing which is about 15% larger than when only considering the direct radiative effect of changes in atmospheric CH_4 concentrations (Shindell et al., 2009). By describing uncertainty in the diffusive carbon uptake, in climate sensitivity, and in ocean heat uptake, our parameter sampling accounts for a large spread in simulated carbon-cycle climate responses. Based on the pathway of anthropogenic and permafrost-induced emission of CO_2 and CH_4, we thus can calculate the change in global mean surface air temperature (see also supplementary information in Allen et al. 2009).

As permafrost regions warm much stronger than the globe as a whole, it is important to account for the polar amplification of temperature change to simulate the warming of permafrost regions. We do this by applying latitude-dependent amplification factors which we infer from an analysis of state-of-the-art climate models (CMIP-5, (Taylor et al., 2011)). This analysis has resulted in typical amplification factors between 1.6 at the southernmost permafrost limit and about 2.3 at the northernmost permafrost limit. By using these scaling factors, we thus can translate our simulated global temperature anomalies into regional warming of high-latitude permafrost regions. Based on these scaled temperatures anomalies, we calculate permafrost degradation in each latitude band.

Supplementary references

Allen, M. R., Frame, D. J., Huntingford, C., Jones, C. D., Lowe, J. A., Meinshausen, M., and Meinshausen, N.: Warming caused by cumulative carbon emissions towards the trillionth tonne, Nature, 458, 1163, 2009.

Arp, C. D., Jones, B. M., Lu, Z., and Whitman, M. S.: Shifting balance of thermokarst lake ice regimes across the Arctic Coastal Plain of northern Alaska, Geophysical Research Letters, 39, L16503, 10.1029/2012GL052518, 2012.

Avis, C. A., Weaver, A. J., and Meissner, K. J.: Reduction in areal extent of high-latitude wetlands in response to permafrost thaw, Nature Geosci, 4, 444-448, 2011.

Beer, C., Fedorov, A. N., and Torgovkin, Y.: Permafrost temperature and active-layer thickness of Yakutia with 0.5-degree spatial resolution for model evaluation, Earth Syst. Sci. Data, 5, 305-310, 10.5194/essd-5-305-2013, 2013.

Boike, J., Kattenstroth, B., Abramova, K., Bornemann, N., Chetverova, A., Fedorova, I., Fröb, K., Grigoriev, M., Grüber, M., Kutzbach, L., Langer, M., Minke, M., Muster, S., Piel, K., Pfeiffer, E. M., Stoof, G., Westermann, S., Wischnewski, K., Wille, C., and Hubberten, H. W.: Baseline characteristics of climate, permafrost and land cover from a new permafrost observatory in the Lena River Delta, Siberia (1998–2011), Biogeosciences, 10, 2105-2128, 10.5194/bg-10-2105-2013, 2013.

Conrad, R., Klose, M., and Claus, P.: Pathway of CH4 formation in anoxic rice field soil and rice roots determined by 13C-stable isotope fractionation, Chemosphere, 47, 797-806, 10.1016/S0045-6535(02)00120-0, 2002.

Friedlingstein, P., Cox, P., Betts, R., Bopp, L., von Bloh, W., Brovkin, V., Cadule, P., Doney, S., Eby, M., Fung, I., Bala, G., John, J., Jones, C., Joos, F., Kato, T., Kawamiya, M., Knorr, W., Lindsay, K., Matthews, H. D., Raddatz, T., Rayner, P., Reick, C., Roeckner, E., Schnitzler, K.-G., Schnur, R., Strassmann, K., Weaver, K., Yoshikawa, C., and Zeng, N.: Climate–Carbon Cycle Feedback Analysis: Results from the C4MIP Model Intercomparison, Journal of Climate, 19, 3337-3353, 10.1175/JCLI3800.1, 2006.

Frolking, S., Roulet, N. T., Moore, T. R., Richard, P. J. H., Lavoie, M., and Muller, S. D.: Modeling northern peatland decomposition and peat accumulation, Ecosystems, 4, 479-498, 2001.

Hugelius, G., Tarnocai, C., Broll, G., Canadell, J. G., Kuhry, P., and Swanson, D. K.: The Northern Circumpolar Soil Carbon Database: spatially distributed datasets of soil coverage and soil carbon storage in the northern permafrost regions, Earth Syst. Sci. Data, 5, 3-13, 10.5194/essd-5-3-2013, 2013.

Jones, M. C., Grosse, G., Jones, B. M., and Walter Anthony, K.: Peat accumulation in drained thermokarst lake basins in continuous, ice-rich permafrost, northern Seward Peninsula, Alaska, Journal of Geophysical Research: Biogeosciences, 117, G00M07, 10.1029/2011JG001766, 2012.

Jorgenson, M. T., Romanovsky, V., Harden, J., Shur, Y., O'Donnell, J., Schuur, E. A. G., Kanevskiy, M., and Marchenko, S.: Resilience and vulnerability of permafrost to climate change, Canadian Journal of Forest Research-Revue Canadienne De Recherche Forestiere, 40, 1219-1236, 2010.

Kessler, M. A., Plug, L. J., and Walter Anthony, K. M.: Simulating the decadal- to millennial-scale dynamics of morphology and sequestered carbon mobilization of two thermokarst lakes in NW Alaska, Journal of Geophysical Research: Biogeosciences, 117, G00M06, 10.1029/2011JG001796, 2012.

Kleinen, T., Brovkin, V., and Schuldt, R. J.: A dynamic model of wetland extent and peat accumulation: results for the Holocene, Biogeosciences, 9, 235-248, 10.5194/bg-9-235-2012, 2012.

Koven, C. D., Riley, W. J., and Stern, A.: Analysis of Permafrost Thermal Dynamics and Response to Climate Change in the CMIP5 Earth System Models, Journal of Climate, 26, 1877-1900, 10.1175/JCLI-D-12-00228.1, 2013.

Lee, H., Schuur, E. A. G., Inglett, K. S., Lavoie, M., and Chanton, J. P.: The rate of permafrost carbon release under aerobic and anaerobic conditions and its potential effects on climate, Global Change Biology, 18, 515-527, 10.1111/j.1365-2486.2011.02519.x, 2012.

Ling, F.: Numerical simulation of permafrost thermal regime and talik development under shallow thaw lakes on the Alaskan Arctic Coastal Plain, Journal of Geophysical Research, 108, 4511-4511, 2003.

Meinshausen, M., Smith, S. J., Calvin, K., Daniel, J. S., Kainuma, M., Lamarque, J., Matsumoto, K., Montzka, S., Raper, S., and Riahi, K.: The RCP greenhouse gas concentrations and their extensions from 1765 to 2300, Climatic Change, 109, 213-241, 2011.

Morgenstern, A., Grosse, G., Günther, F., Fedorova, I., and Schirrmeister, L.: Spatial analyses of thermokarst lakes and basins in Yedoma landscapes of the Lena Delta, The Cryosphere, 5, 849-867, 10.5194/tc-5-849-2011, 2011.

Myhre, G., Highwood, E. J., Shine, K. P., and Stordal, F.: New estimates of radiative forcing due to well mixed greenhouse gases, Geophys. Res. Lett., 25, 2715-2718, 1998.

Olefeldt, D., Turetsky, M. R., Crill, P. M., and McGuire, A. D.: Environmental and physical controls on northern terrestrial methane emissions across permafrost zones, Global Change Biology, 19, 589-603, 10.1111/gcb.12071, 2013.

Romanovsky, V. E., Smith, S. L., and Christiansen, H. H.: Permafrost thermal state in the polar Northern Hemisphere during the international polar year 2007–2009: a synthesis, Permafrost and Periglacial Processes, 21, 106-116, 10.1002/ppp.689, 2010.

Scanlon, D., and Moore, T.: Carbon dioxide production from peatland soil profiles: The influence of temperature, oxic/anoxic conditions and substrate, Soil Science, 165, 153-160, 2000.

Schaphoff, S., Heyder, U., Ostberg, S., Gerten, D., Heinke, J., and Lucht, W.: Contribution of permafrost soils to the global carbon budget, Environmental Research Letters, 8, 014026, 2013.

Schirrmeister, L., Grosse, G., Wetterich, S., Overduin, P. P., Strauss, J., Schuur, E. A. G., and Hubberten, H.-W.: Fossil organic matter characteristics in permafrost deposits of the northeast Siberian Arctic, Journal of Geophysical Research: Biogeosciences, 116, G00M02, 10.1029/2011JG001647, 2011.

Segers, R.: Methane production and methane consumption: a review of processes underlying wetland methane fluxes, Biogeochemistry, 41, 23-51, 1998.

Shindell, D. T., Faluvegi, G., Koch, D. M., Schmidt, G. A., Unger, N., and Bauer, S. E.: Improved Attribution of Climate Forcing to Emissions, Science, 326, 716-718, 10.1126/science.1174760, 2009.

Strauss, J., Schirrmeister, L., Grosse, G., Wetterich, S., Ulrich, M., Herzschuh, U., and Hubberten, H.-W.: The deep permafrost carbon pool of the Yedoma region in Siberia and Alaska, Geophysical Research Letters, 40, 2013GL058088, 10.1002/2013GL058088, 2013.

Taylor, K. E., Stouffer, R. J., and Meehl, G. A.: An Overview of CMIP5 and the Experiment Design, Bulletin of the American Meteorological Society, 93, 485-498, 10.1175/BAMS-D-11-00094.1, 2011.

van Huissteden, J., and Dolman, A.: Soil carbon in the Arctic and the permafrost carbon feedback, Current Opinion in Environmental Sustainability, 4, 545-551, 2012.

Walter Anthony, K. M., Zimov, S. A., Grosse, G., Jones, M. C., Anthony, P. M., Iii, F. S. C., Finlay, J. C., Mack, M. C., Davydov, S., Frenzel, P., and Frolking, S.: A shift of thermokarst lakes from carbon sources to sinks during the Holocene epoch, Nature, 511, 452-456, 10.1038/nature13560, 2014.

Yi, S., Wischnewski, K., Langer, M., Muster, S., and Boike, J.: Freeze/thaw processes in complex permafrost landscapes of northern Siberia simulated using the TEM ecosystem model: impact of thermokarst ponds and lakes, Geosci. Model Dev., 7, 1671-1689, 10.5194/gmd-7-1671-2014, 2014.

Yoshikawa, K., and Hinzman, L. D.: Shrinking thermokarst ponds and groundwater dynamics in discontinuous permafrost near council, Alaska, Permafrost and Periglacial Processes, 14, 151-160, 10.1002/ppp.451, 2003.

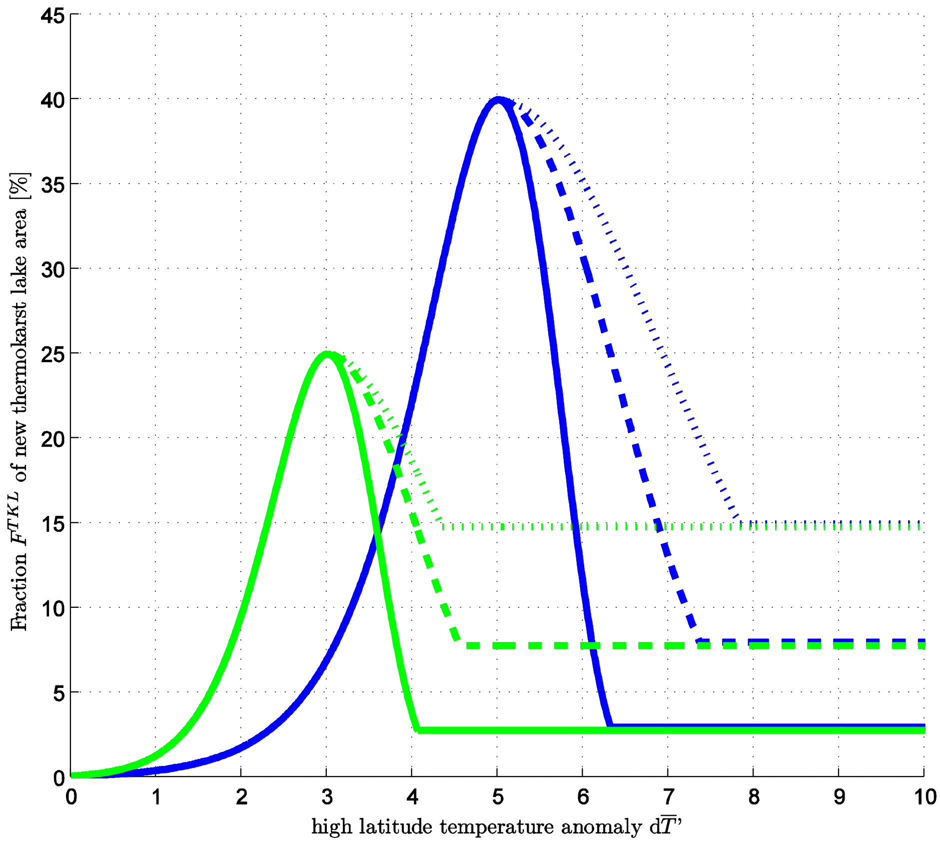

Fig.S1: Temperature dependency of newly formed thermokarst lake area fractions. The figure illustrates the increase and decrease of the new thermokarst lake area fraction $\mathrm{F}^{\mathrm{TKL}}$ (as percentage of the total permafrost area in each latitude band) with rising high latitude surface air warming $\mathrm{d}\overline{\mathrm{T}}'$. Curves are shown for two different choices of maximum thermokarst lake extents $\mathrm{F}^{\mathrm{TKLmax}}$ (green: 25%, blue: 40%) and corresponding warming $\mathrm{d}\overline{\mathrm{T}}'^{\mathrm{TKLmax}}$ (green: 3°C, blue: 5°C). The different line styles illustrate the latitudinal dependency of drainage for warming above $\mathrm{d}\overline{\mathrm{T}}'^{\mathrm{TKLmax}}$ (solid: southern permafrost limit, dashed: mid permafrost latitude, dotted: northern permafrost limit).